RESEARCH ARTICLE

Magnetocardiography Detection and Source Localization From Multiple Sources Using Magnetoimpedance Principle in Controlled Environment

K. V. ANU [ID][1]**, VIKAS R. BHAT** [ID][1]**, H. RESHMA**[2]**, AND H. ANITHA** [ID][3]**, (Member, IEEE)**

[1]Department of Biomedical Engineering, Manipal Institute of Technology, Manipal Academy of Higher Education, Manipal 576104, India
[2]Department of Electronics and Communication Engineering, Manipal Institute of Technology, Manipal Academy of Higher Education, Manipal 576104, India
[3]School of Computer Engineering, Manipal Institute of Technology, Manipal Academy of Higher Education, Manipal 576104, India

Corresponding authors: Vikas R. Bhat (vikas.bhat@manipal.edu) and H. Anitha (anitha.h@manipal.edu)

ABSTRACT Recent advances in non-invasive cardiac imaging techniques have highlighted the potential of Magnetocardiography (MCG) as a powerful diagnostic tool. However, existing approaches face significant challenges in accurately localizing and characterizing cardiac electrical sources. This study presents an innovative methodology for cardiac source localization using magnetocardiography based on the magnetoimpedance principle, addressing these limitations through an experimental framework and sophisticated computational approaches. This work has established a novel lead field matrix computation methodology that shows the relationship between source currents and resulting magnetic fields. The forward problem was solved using known source configurations and validated against experimental measurements. For the inverse problem, three mathematical approaches were implemented: Minimum Norm Estimation (MNE), Empirical covariance, and Gaussian Process Variance methods. Results demonstrate that the overall experimental setup successfully replicates key aspects of cardiac electromagnetic activity, with the MI sensor array providing sufficient spatial and temporal resolution for accurate source localization. The novel lead field computation method significantly improved source reconstruction accuracy compared to conventional approaches. This work establishes a foundation for cost-effective high-sensitivity magnetocardiographic systems that could enhance clinical cardiac diagnostics without the need for magnetically shielded environments.

INDEX TERMS Forward problem, inverse problem, lead field, lead field matrix, magnetocardiography, magneto-impedance sensors.

I. INTRODUCTION

The electrical activity of the human heart, sequentially beats through its specialized conduction system, generates both electrical and magnetic fields that can be measured non-invasively, giving rise to two complementary diagnostic modalities: electrocardiography (ECG) and magnetocardiography (MCG) [1]. ECG has been the traditional gold standard for cardiac diagnostic imaging since Einthoven's pioneering work in the early 20th century [2]. MCG has emerged as a powerful alternative offering distinct advantages in spatial resolution and source localization capability. The human heart, a remarkable electromechanical organ, generates complex electrical activity that manifests as both electrical and magnetic fields that are detectable from the body surface [3]. The fundamental principle underlying both modalities stems from the coordinated ion movements across cardiac cell membranes, particularly the synchronized flow of

The associate editor coordinating the review of this manuscript and approving it for publication was Andrea De Marcellis [ID].

Na^+, K^+ and Ca^{2+} ions, which generates action potentials and subsequent propagation through the cardiac conduction system. These ionic currents, manifesting as both primary (intracellular) and secondary (extracellular) currents, create time-varying electromagnetic fields [Fig. 1] governed by Maxwell's equations and specifically by the Biot-Savart law:

$$\mathbf{B}(\mathbf{r}) = (\mu_0/4\pi) \int \frac{\mathbf{J}(\mathbf{r}') \times (\mathbf{r} - \mathbf{r}')}{|\mathbf{r} - \mathbf{r}'|^3} dr' \qquad (1)$$

where $\mathbf{B}(\mathbf{r})$ represents the magnetic field at position $\mathbf{r}$, $\mathbf{J}(\mathbf{r}')$ denotes the current density at source position $\mathbf{r}'$, and μ_0 is the permeability of free space.
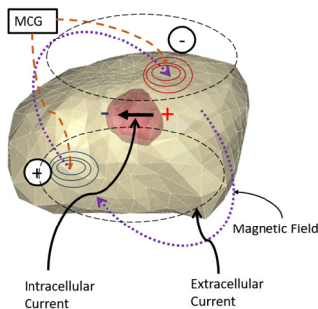

FIGURE 1. Ionic movement through cardiac nodes creates intracellular currents (solid black arrows) that generate extracellular currents (dotted black arrows) when passing through the cell surface. As the heart acts as a conductive medium, these continuous current flows produce detectable magnetic fields (purple), which can be measured non-invasively using magnetocardiography (MCG) methodology.

MCG has demonstrates superior capabilities in source reconstruction compared to ECG primarily due to the fundamental physics of magnetic fields [4], which experience minimal distortion when passing through biological tissues, unlike electrical potentials that are significantly affected by varying tissue conductivities and the low conductivity of the bone and skin layers. This advantage becomes particularly pronounced in detecting tangential currents and deep sources within the myocardium, areas where ECG shows limited sensitivity. The detection of these extremely weak cardiac magnetic fields (typically $pT - fT$) has evolved from early induction coil measurements to sophisticated modern technologies, including: (*i*) Superconducting Quantum Interference Devices (SQUIDs), (*ii*) Optically pumped magnetometers (OPMs), (*iii*)High-sensitivity fluxgate sensors and (*iv*) Magneto-impedance sensors (MI sensors) While SQUID sensors are widely used due to their femtotesla-range sensitivity, they present significant drawbacks: they are bulky, require controlled temperature environments, fully shielded rooms, and involve high initial and maintenance costs. Each technology offers specific advantages in terms of sensitivity, cost, and operational requirements. Notably, Magneto-impedance sensors (MI sensors) [5] feature an amorphous wire component which changes its resistance with respect to an external magnetic field, producing a voltage

signal. These sensors require negligible shielding, offer high sensitivity, and have a noise floor of $200pT/\sqrt{Hz}$.

MCG source reconstruction process encompasses two fundamental mathematical challenges: the forward and inverse problems [6]. The reconstruction of cardiac electrical activity from MCG measurements involves addressing these challenges systematically:

A. FORWARD PROBLEM

Expressed as $\mathbf{B} = \mathbf{LJ}$, involves calculating the magnetic field distribution from known cardiac sources through the lead field matrix $\mathbf{L}$, which establishes geometrical relationship between source and sensor.

B. INVERSE PROBLEM

Focuses on reconstructing cardiac sources from measured magnetic fields, formulated as $\mathbf{J} = \mathbf{L}^\dagger \mathbf{B}$, though this simplification belies the complexity of the ill-posed nature of the problem due to its non-unique solutions.

The lead field theory [7] provides a crucial mathematical framework for relating source activities to measured signals, taking into account sensor positions, anatomical structure, and tissue properties. The inverse problem requires sophisticated regularization techniques and constraints based on physiological and anatomical knowledge. The source model in MCG can effectively represent cardiac activity through various approaches, including distributed current dipoles [8], equivalent current densities [9], or anatomically constrained source distributions [10], with recent advances in realistic heart modeling [11] and 3D printing enabling more accurate source representations.

Previous research has made significant contributions across these domains, from improving sensor technologies and array configurations to developing advanced algorithms for source reconstruction and noise reduction, with notable works by Cohen et al. [12], Wikswo and Barach [13], and others establishing the fundamental principles and clinical applications of MCG. This paper builds upon this foundation and presents an innovative methodology for cardiac source localization using magnetocardiography based on the magnetoimpedance (MI) principle, addressing these limitations through an experimental framework and sophisticated computational approaches. While this study utilizes a controlled laboratory environment with a 3D-printed cardiac phantom to establish the fundamental principles and validate this methodology, it represents an essential first step toward clinical translation. The controlled environment allows for precise validation of this computational approaches with known ground truth, which would be challenging with real cardiac data where the true source distributions are unknown. The work contributes to the field by:

i. Demonstrating the feasibility of MI-based MCG systems as an alternative to expensive SQUID-based systems.

ii. Novel methodologies for computing the lead field matrix using MI sensor measurements.

iii. Providing a comprehensive comparison of inverse problem solution methods specifically tailored for MCG applications

iv. establishing a validated framework that can be extended to more complex, realistic scenarios in future studies.

This comprehensive framework addresses fundamental challenges in MCG source reconstruction while establishing a foundation for future advancements in cardiac diagnostics and research. The methodology combines physical modeling, advanced sensing technology, and sophisticated mathematical frameworks to enhance the understanding of cardiac electrical dynamics and improve diagnostic capabilities in clinical settings.

II. LITERATURE REVIEW

A. MAGNETOCARDIOGRAPHY DEVELOPMENT AND APPLICATIONS

Magnetocardiography has evolved significantly since its first recording by Baule and McFee in 1963, who detected cardiac magnetic fields using induction coils. The introduction of SQUID sensors in the early 1970s by Cohen et al. [12] revolutionized the field, enabling routine detection of the weak magnetic fields produced by the heart. Subsequent work by Williamson and Kaufman [14] demonstrated the potential clinical utility of MCG in identifying abnormal cardiac conditions. Modern clinical applications of MCG include detection of ischemia, risk stratification in coronary artery disease, localization of accessory pathways, and identification of ventricular arrhythmia substrates [15]. A comprehensive review by Fenici et al. [16]highlighted the potential advantages of MCG over ECG in these contexts, particularly for conditions where spatial localization is critical. Despite these promising applications, the widespread adoption of MCG has been limited by practical considerations. As noted by Koch [17], conventional SQUID-based systems require specialized infrastructure, including magnetically shielded rooms and cryogenic cooling systems, which restrict their use to specialized research centres [4]. These limitations have motivated the search for alternative sensing technologies that could make MCG more accessible.

B. PRINCIPLES AND APPLICATIONS OF MAGNETO-IMPEDANCE SENSORS

magneto-impedance (MI) sensors operate on the principle that the impedance of certain soft magnetic materials changes significantly in the presence of an external magnetic field. This effect, first introduced by Panina and Mohri [18], occurs due to the interaction between an alternating current flowing through the material and the dynamic permeability of the material, which is highly sensitive to external magnetic fields. The fundamental physics of the MI effect was further elaborated by Knobel and Pirota [19], who described the relationship between material composition, geometry, and

sensitivity. Subsequent work by Honkura [20] demonstrated practical sensor implementations achieving sensitivities in the nanotesla range, with continuing improvements in subsequent years. Uchiyama et al. [21] first proposed the application of MI sensors to biomagnetism, demonstrating the detection of magnetic fields from isolated animal hearts. This was followed by work from Nakayama et al. [22], who achieved detection of human cardiac magnetic fields using an array of MI sensors in a partially shielded environment. More recently, Wang et al. [23]demonstrated a compact MCG system using MI sensors that could operate in minimally shielded environments, suggesting the feasibility of clinical applications. Despite these advances, the use of MI sensors in MCG presents unique challenges. Unlike SQUIDs, which provide direct measurement of magnetic flux, MI sensors respond to field strength through impedance changes, requiring different signal conditioning and calibration approaches [24]. Additionally, MI sensors may exhibit non-linear responses and cross-field sensitivity that must be accounted for in measurement systems.

C. FORWARD AND INVERSE PROBLEMS IN MAGNETOCARDIOGRAPHY

The forward problem in biomagnetism involves calculating the magnetic field distribution from known source configurations. Early work by Sarvas [7] established the mathematical framework for computing magnetic fields from current dipoles in a spherical conductor, which has been widely used in MCG forward calculations. More sophisticated approaches incorporate realistic torso models using boundary element or finite element methods, as described by Stenroos et al. [25]. This forward problem formulate a mathematical relationship between the known electrical activity as well as the unknown surface magnetic field The inverse problem — reconstructing source currents from measured magnetic fields — presents greater challenges due to its inherently ill-posed nature. Hämäläinen and Ilmoniemi [26] introduced the minimum norm estimation (MNE) approach, which seeks the current distribution with minimum L2 norm that explains the measured data. This approach has been widely adopted in both magnetoencephalography (MEG) and MCG. Various refinements to basic inverse methods have been proposed to improve localization accuracy. Weighted minimum norm approaches, as described by Gorodnitsky et al. [27] in their FOCUSS algorithm, iteratively adjust source weights to promote focal solutions. Bayesian approaches, such as those described by Tarantola [28], incorporate prior information about source distributions to constrain solutions. More recently, Empirical Bayesian methods, such as the Empirical covariance approach described by Phillips et al. [29] and Gaussian process variance methods detailed by Wipf and Nagarajan [30], have shown promise in bioelectromagnetic source localization by automatically determining optimal regularization parameters from the data. The validation of inverse solutions remains challenging. Simulated data
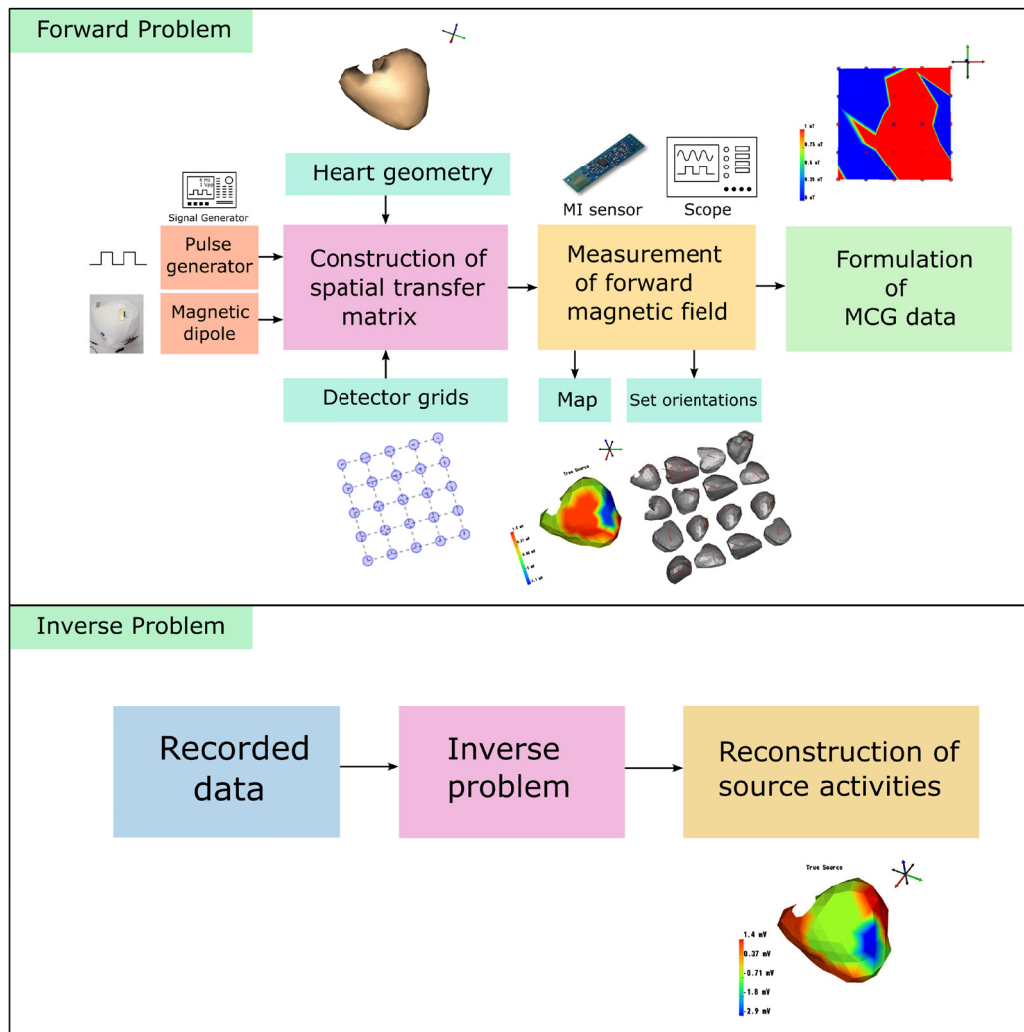
FIGURE 2. Block diagram illustrating the complete experimental workflow for magnetocardiography source localization. The system comprises four main components: (1) Source simulation using a copper coil positioned at 16 anatomically relevant ventricular locations on a 3D-printed heart model, (2) Magnetic field detection using a single MI sensor sequentially positioned at 25 grid locations, (3) Data acquisition and signal processing including amplification, filtering, and digitization, and (4) Computational analysis incorporating forward problem solution through lead field matrix computation and inverse problem solution using three distinct methods (MNE, Empirical Bayesian, and Gaussian Process). Arrows indicate data flow direction, with feedback loops showing the iterative optimization processes involved in regularization parameter selection and source reconstruction accuracy assessment.

provides known ground truth but may not capture real-world measurement conditions. Physical phantoms with controlled sources offer more realistic validation but have historically been limited in anatomical detail and physiological realism. Studies by Jeremic et al. [31] have emphasized the need for improved experimental validation methods that bridge the gap between computational models and in vivo measurements.

D. EXPERIMENTAL APPROACHES TO MCG VALIDATION

Physical phantoms for validating bioelectromagnetic measurements have evolved from simple geometric shapes to more anatomically realistic models. Early work by Brauer et al. [32] utilized spherical phantoms with embedded dipole sources to validate MEG inverse methods. Subsequent studies by Leahy et al. [33] extended this approach to more complex geometries and multiple sources. The advent of 3D printing technology has enabled the creation of more anatomically accurate phantoms. Kim et al. [34] demonstrated the use of 3D-printed skull models for validating EEG source localization. In the cardiac domain, Jekie et al [35] and Stevenson et al. [34] created a torso phantom with realistic conductivity properties for validating ECG measurements, but comparable phantoms for MCG validation have been limited. Controlled phantom studies are essential for MCG method development and validation because they provide known ground truth

for source locations and activities, which is impossible to obtain in real cardiac measurements. This approach allows for systematic evaluation of reconstruction accuracy and method performance under controlled conditions, establishing the foundation for future clinical applications.

The use of controlled current sources to mimic cardiac electrical activity presents additional challenges. While simplified dipole sources provide mathematical tractability, they do not capture the distributed nature of cardiac activation. More realistic approaches by Jekic et al. [36] have utilized multiple current sources with physiologically timed activation sequences, but these have primarily been applied to ECG rather than MCG validation.

III. MATERIALS AND METHODS

A. PROPOSED METHODOLOGY

Fig. 2 illustrates that the experimental framework is designed to systematically reconstruct the activity of the heart source responsible for the magnetic field distribution in the thorax region under controlled conditions. The experimental framework incorporating a source model, a grid-mounted magnetic induction (MI) detector, and a lead field calculation established a practical and realistic framework for solving forward and inverse problems in magnetocardiography (MCG). Approach assumes that the source activity is exactly repeatable and there are no drifts in the sensor or environment between measurements. While this sequential approach is acceptable for a phantom study, it represents a limitation for real-time measurements as one cannot perform this sequential sampling during a real heartbeat. The viability of this approach rests on the assumption of identical repeated pulses and a static system. After data acquisition for further processing, comprehensive computational analysis and visualization software like MATLAB, ECGSIM, and SCIRUN were also incorporated. The forward problem can be mathematically formulated as:

$$\mathbf{B_m}(\mathbf{r_m}, t) = \mathbf{A}(\mathbf{r_m}, \mathbf{r_q}) \cdot \mathbf{s}(\mathbf{r_q}, t) \quad (2)$$

where $\mathbf{B}_m(\mathbf{r_m}, t)$ represents the magnetic field measured at position $\mathbf{r}_m$ at time t, $\mathbf{A}(\mathbf{r_m}, \mathbf{r_q})$ denotes the practical lead field matrix relating source positions $\mathbf{r}_q$ to measurement positions $\mathbf{r}_m$, and $\mathbf{s}(\mathbf{r_q}, t)$ describes the source current density at position $\mathbf{r}_q$ at time t.

Consequently, the inverse problem solution can be expressed as:

$$\mathbf{s}_{rec}(\mathbf{r_q}, t) = \mathbf{A}^{\dagger}(\mathbf{r_m}, \mathbf{r_q}) \cdot \mathbf{B}_m \quad (3)$$

where $S_{rec}(\mathbf{r_q}, t)$ represents the reconstructed source current density, and $\mathbf{A}^{\dagger}(\mathbf{r_m}, \mathbf{r_q})$ indicates the pseudo inverse of lead field. Summarized steps of the work are given below:

1) A copper coil (90 turns, 20 mm length) powered with a 6 Hz square wave, used as a source model positioned at sixteen ventricular locations systematically. q is considered as the index of the selected node (1)-(16)

2) Magnetic field arising from the coil is measured through a single MI sensor (Aichi Steel MI-CB-1DJ-S-B [37])

sequentially positioned at 25 grid locations. m is the index of the corresponding sensor position (1)-(25)

3) Magnetic field pulses $\mathbf{c}(\mathbf{r}_q, t)$ measured as the coil activates at each of the 16 node locations

4) Lead field matrix $\mathbf{A}(\mathbf{r}_m, \mathbf{r}_q)$ computed from 16 source-25 sensor measurements.

5) Magnetic field $\mathbf{B}_M(\mathbf{r}_m, t)$ solved using linear relation between the known source $\mathbf{s}(\mathbf{r}_q, t)$ and $\mathbf{A}(\mathbf{r}_m, \mathbf{r}_q)$.

6) Source activity $\hat{\mathbf{s}}$, $\mathbf{s}_{rec}(\mathbf{r}_q, t)$ reconstructed using inverse matrix $\mathbf{A}^{\dagger}(\mathbf{r}_m, \mathbf{r}_q)$
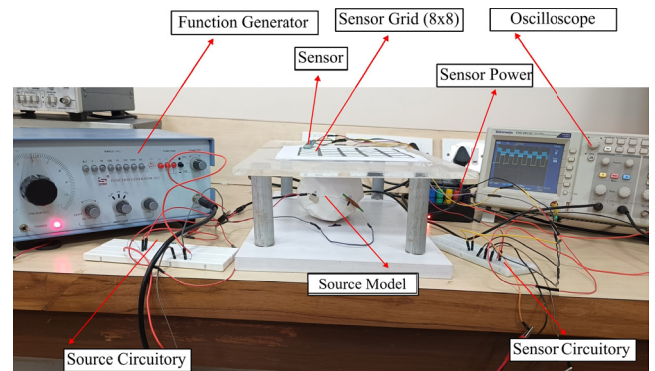

FIGURE 3. Table top experimental setup.

B. EXPERIMENTAL CONFIGURATION DETAILS

1) HEART SOURCE AND COIL CONFIGURATIONS

Anatomically accurate 3D printed heart model was developed as the foundation for experimental investigations with measurements of $10.63 \times 13.03 \times 9.27$ cm [38]. Heart's structural information was extracted from ECGSIM [39], a simulation tool for studying cardiac electrophysiology. The model featured 257 distinct nodes distributed throughout the ventricular structure (Fig. 4).
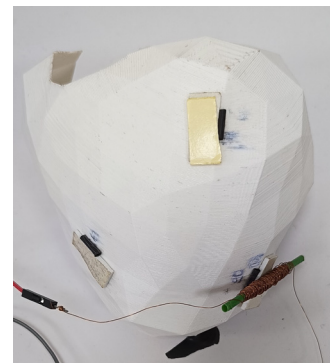

FIGURE 4. 3D printed model of the ventricular surface of the heart, which contains 256 discretized nodes and the copper source coil.

To reduce complexity while maintaining anatomical relevance, sixteen ventricular nodes were strategically selected based on established cardiac conduction pathways. These nodes were strategically positioned to monitor critical areas of ventricular activation: four nodes in the septal region, six
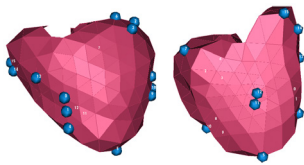
FIGURE 5. Selection of 16 anatomical points on ventricular surface displayed using SCIRUN.

nodes across the left ventricular free wall, four nodes within the right ventricular wall, and two nodes at the apex.

The spatial distribution of these 16 selected nodes was visualized using SCIRUN software [40] as shown in Fig. 5, with detailed positional information presented in Table 1.

A custom induction coil (90 turns, 0.58 mm wire diameter, 20 mm length) was utilized to generate localized magnetic fields at each node. The coil was driven with a 6 Hz pulse signal rather than a Transmembrane potential wave (TMP) better to represent the discrete activation events in ventricular electrophysiology. This approach allowed the sharp initial peak of each pulse to effectively simulate the activation moment of individual ventricular nodes, providing a more physiologically accurate representation of the sequential activation pattern during ventricular depolarization in controlled environment. Fig. 6 demonstrates the comparison of TMP along with the pulse signal.
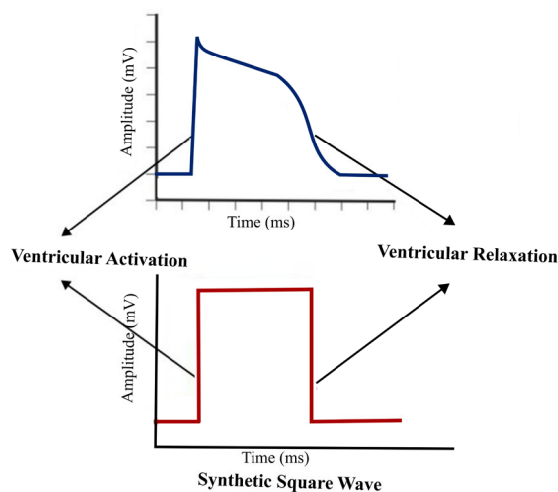

FIGURE 6. Comparison between the transmembrane potential (TMP) signal (blue) and the pulse signal (red).

The magnetic field generated by the coil was calculated using Ampere's law for a finite solenoid, with appropriate correction factors applied to account for edge effects. For specific configuration with a current of 39 μA, the calculation yielded a magnetic field strength of approximately 62.6 nT at the measurement location. This field strength, while relatively small, falls within the range of magnetic fields naturally produced by the human heart (pT range), ensuring
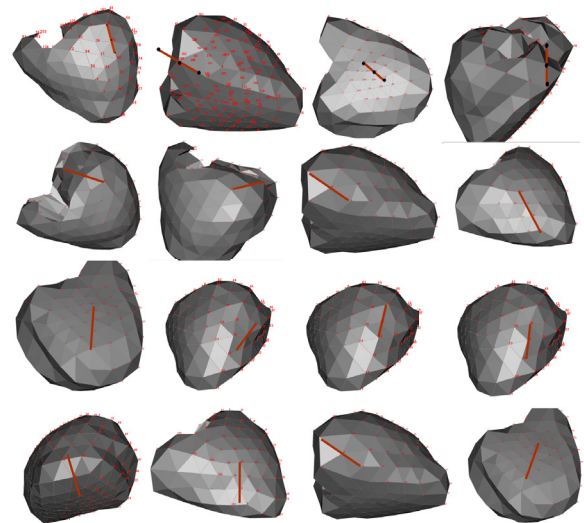

FIGURE 7. Coil (Red line) positioning across 16 cardiac nodes on 3D heart model, shown from multiple angles.

the experimental model closely approximated physiological conditions.

The coil orientation was maintained consistently across all 16 node positions, with the coil axis oriented in different directions determined through experimental validation to identify the most prominent data acquisition positions. Copper coil orientation strategy was determined through systematic experimental validation to identify optimal magnetic field generation patterns at each ventricular node. At each of the 16 selected ventricular positions, the coil axis was oriented according to unit vectors computed from the local cardiac conduction pathway geometry (Table1). These orientation vectors were derived from the nearest coil end-point locations, ensuring that the generated magnetic dipole moment aligned with physiologically relevant current flow directions during ventricular depolarization. As illustrated in Fig. 8, this source model demonstrates the experimental setup where ''coil 1'' and ''coil 2'' represent the same physical coil positioned at different locations. The coil was initially placed at node 1 (indicated in red) to generate magnetic field B1, then systematically repositioned to node 2 (indicated in green) to produce magnetic field B2. This sequential positioning approach was applied across all measurement locations.
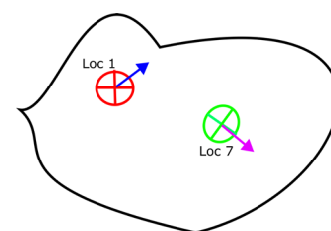

FIGURE 8. Graphical representation of the experimental source, a heart model in which two nodes are shown and B1 and B2 are same coil placed with respect to the activation time of node 1 and node 2 in different orientations.

TABLE 1. Selected node information with activation times.

Node Number	Node Index	Location [x,y,z]	Activation time (ms)	Orientation [x, y, z]
1	17	0.0891, 0.0409, -0.0133	33	-0.9888, -0.1300, -0.0728
2	63	0.0889, 0.0471, -0.0233	38	-0.3753, -0.9195, 0.1169
3	81	0.0048, 0.0630, -0.0248	39	-0.4172, -0.8092, -0.4137
4	45	0.0207, 0.0495, 0.0426	40	-0.5794, 0, -0.8150
5	35	0.0377, 0.0541, 0.0441	42	0.2998, 0.2581, -0.9184
6	6	0.0896, 0.0546, -0.0355	43	0.4995, 0.4540, -0.7378
7	44	0.0322, 0.0360, 0.0427	44	0.9240, 0.2176, -0.3145
8	92	-0.0115 , 0.0218, -0.0133	46	0, 1, 0
9	23	-0.0113, 0.0409, -0.0133	46	0.7384, 0.3540, -0.5739
10	76	0.0383, 0.0934, 0.0020	51	-0.8504, 0.4310, -0.3016
11	75	0.0234, 0.0889, -0.0005	52	0.9379, 0.2882, -0.1930
12	117	0.0473, 0.0500, -0.0453	55	0.2513, 0.7307, -0.6348
13	9	0.0473, 0.0409, -0.0450	61	-0.0121, 0.2374, 0.9713
14	28	0.0871, 0.0120, -0.0133	67	0, 0.9941, -0.1086
15	99	0.0745, -0.0137, -0.0279	78	0.2956, 0.2148, -0.9308
16	101	0.0586, -0.0252, -0.0326	93	0.2368, 0.2805, -0.9302
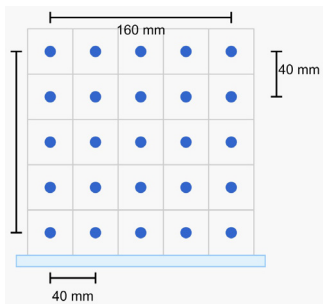
FIGURE 9. 5 × 5 sensor grid where adjacent sensor locations set with 40 mm gap.

2) MAGNETO-IMPEDANCE SENSOR CONFIGURATIONS

Magneto-impedance (MI) sensors (Aichi Steel MI-CB-1DJ-S-B [37], sensitivity: $5V/\mu T$, frequency response: $0.1\ Hz$ to $10kHz@ - 3dB$, noise floor: $10pT/\sqrt{Hz}$ at 1 Hz) were utilized for high-sensitivity detection of the magnetic fields. MI sensor sensitivity direction was precisely aligned normal to the measurement plane to optimize detection of the dominant magnetic field component generated by the cardiac source model. This perpendicular orientation maximizes sensor response to the expected dipolar magnetic field patterns while minimizing sensitivity to orthogonal field components that could introduce measurement artifacts and cross-coupling effects.

3) SENSOR ARRAY CONFIGURATION

MI sensors were arranged in a 5×5 planar grid with 40 mm spacing between adjacent sensors, creating a 24 × 24 mm measurement area which represents in Fig. 9. This grid was placed on a non-magnetic acrylic plate positioned 50 mm above the ventricular model to capture the propagating magnetic fields which mimic the actual heart-thorax distance.

4) DATA ACQUISITION SYSTEM

MI sensor was sequentially positioned at 25 different locations in a 5×5 grid pattern. For each of the 16 ventricular

nodes under investigation, the single MI sensor was systematically repositioned across the 25 predetermined grid locations to capture the complete magnetic field pattern generated by that node. Signal from the MI sensor was digitized using a digital oscilloscope for each measurement position along with the simultaneous pulse data. For each combination of node excitation (16 locations) and sensor position (25 locations), 2500 time samples received.

C. ENVIRONMENTAL CONSIDERATIONS AND SETUP VALIDATION

To ensure measurement accuracy and repeatability, the experimental setup was conducted in a controlled laboratory environment. The non-magnetic acrylic mounting system eliminated potential interference from ferromagnetic materials. Signal conditioning included appropriate filtering to remove high-frequency noise while preserving the cardiac signal bandwidth of interest (0.1-60 Hz). Calibration procedures verified sensor response linearity across the expected magnetic field range.

D. LEAD FIELD MATRIX COMPUTATION

The lead field matrix represents the fundamental mathematical relationship between cardiac source activities and the resulting magnetic field measurements [41], serving as the cornerstone of the forward and inverse problem solutions. Here, the current work uses MI sensors to construct the lead field.

1) THEORETICAL FOUNDATION

Theoretical foundation of magnetocardiography detection system is based on the fundamental principles of electromagnetic field theory and its application the measurements of cardiac electrical activity. This experimental setup comprises a sophisticated 25-slot sensor array configuration, with each slot sequentially occupied by a specialized MI sensor. This precise arrangement enables comprehensive spatial mapping of magnetic field distributions generated by simulated cardiac

sources. The sensor array systematically captures magnetic field signatures at multiple temporal instances for each activated node, ensuring detailed characterization of the field's temporal evolution.

A current-carrying coil representing a cardiac dipole source, the magnetic field at a measurement point is given by:

$$\mathbf{B}(\mathbf{r}) = \frac{\mu_0 N \mathbf{I} \mathbf{r}^2}{2(\mathbf{r}^2 + a^2)^{3/2}} \tag{4}$$

where $\mathbf{B}(\mathbf{r})$ represents the magnetic field strength at a distance $\mathbf{r}$ from the coil center, μ_0 is the permeability of free space ($4\pi \times 10^{-7}$ H/m), N denotes the number of turns in the coil, $\mathbf{I}$ represents the current flowing through the coil, and a is the radius of the coil. This fundamental equation accounts for the three-dimensional nature of magnetic field propagation and the geometric constraints imposed by the experimental setup.

For situations where the measurement distance significantly exceeds the coil radius ($a \ll r$), the magnetic field equation can be simplified to:

$$\mathbf{B}(\mathbf{r}) = \frac{\mu_0 \mathbf{m}}{2\pi \mathbf{r}^3} \tag{5}$$

where $\mathbf{m} = N\mathbf{I}\pi a^2$ represents the magnetic moment of the coil. This simplification proves particularly useful in experimental contexts, where sensor distances are typically much larger than the source coil dimensions.

2) LEAD FIELD MATRIX FORMULATION

The computational method in this approach involves the development and implementation of the lead field matrix $\mathbf{A}$, which establishes the fundamental mapping between cardiac source locations and magnetic field measurements at the sensors. Under the assumption of $a \ll r$, the lead field matrix is derived through the relationship:

$$\mathbf{A}_m = \mathbf{B}(\mathbf{r}) \times \frac{\mathbf{r}}{2} \tag{6}$$

where, $\mathbf{r} = |\mathbf{r}_m - \mathbf{r}_q|$ defines the spatial relationship between measurement points ($\mathbf{r}_m$) and source locations ($\mathbf{r}_q$), $\mathbf{B}(\mathbf{r})$ represents the magnetic field strength at the measurement points and th factor $\frac{\mathbf{r}}{2}$ accounts for the geometric relationship between source and measurement locations.

For experimental configuration with 16 source locations and 25 measurement points, we constructed a 16 × 25 lead field matrix. Each element A_{ij} represents the sensitivity of the jth sensor to the ith source, incorporating both the distance-dependent field attenuation and the geometric relationship between sources and sensors.

Fig. 10 presents a schematic representation of the fundamental electromagnetic principles of experimental setup. The diagram shows a circular current-carrying coil of radius a representing a cardiac dipole source positioned at location $\mathbf{r}_q$. The magnetic sensor at position $\mathbf{r}_m$ measures the resulting magnetic field $\mathbf{B}(\mathbf{r})$ generated by the source. The distance $\mathbf{r}$ connects the source and sensor positions, playing a critical role in field strength calculations. The magnetic

moment m of the coil, shown as a vertical green vector, depends on the coil parameters (current, turns, and area) and determines the field's magnitude and orientation. The lead field $\mathbf{A}_m$, represented by the red arrow, encapsulates the sensitivity relationship between the specific source-sensor pair, incorporating both the field strength at distance r and the geometric factors of experimental configuration. This visualization elucidates how the lead field matrix elements are constructed for each of the 16 source locations and 25 sensor positions. Computation of this lead field matrix followed a systematic procedure:
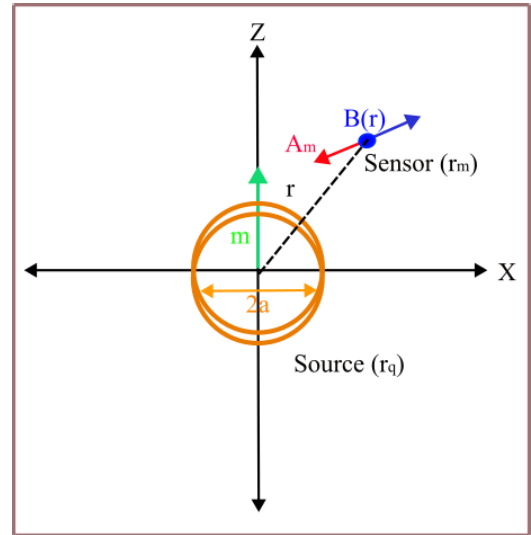

FIGURE 10. Theoretical representation of the source-sensor relationship in magnetocardiography. The diagram illustrates a current-carrying coil source at position r_q with radius a and magnetic moment **m**, generating a magnetic field B(r) measured at sensor position r_m.

E. FORWARD PROBLEM

This lead field matrix serves as a crucial bridge between cardiac source dynamics and observed magnetic field patterns, enabling both forward and inverse problem solutions in experimental framework. The forward problem solution is expressed through the linear mapping equation:

$$\mathbf{B}(\mathbf{r}_m, t) = \mathbf{A}(\mathbf{r}_m, \mathbf{r}_q) \cdot \mathbf{s}(\mathbf{r}_q, t) \tag{7}$$

where $\mathbf{s}(\mathbf{r}_q, t)$ represents the source signal configuration at time t. This comprehensive mathematical framework provides the foundation for predicting magnetic field distributions from known source configurations, essential for validating the experimental setup and calibrating the sensor array.

The integration of these equations within experimental framework enables precise characterization of cardiac electrical activity through non-invasive magnetic field measurements. The matrix formulation explicitly maps the relationship between the heart surface potentials and the body surface measurements through the transfer matrix, providing

Algorithm 1 Lead Field Matrix Construction From Experimental Setup

---

1: Determine the 3D coordinates of all 16 source positions c_1 to c_{16} within the ventricular model and the 25 sensor positions r_1 to r_{25} in the measurement grid.
2: **for** each source position c_i where $i = 1$ to 16 **do**
3:   Activate the coil at c_i using a 6 Hz, 20 mA current pulse.
4:   Simultaneously record the magnetic field response at all sensor positions r_j, where $j = 1$ to 25.
5: **end for**
6: Filter the raw signals to remove environmental noise and system artifacts.
7: Time-align all signals with respect to the source activation sequence.
8: **for** each source-sensor pair (c_i, r_j) **do**
9:   Extract the peak magnetic field value A_{ij}^{raw}.
10:   Compute the Euclidean distance $d_{ij} = \|r_j - C_i\|$.
11:   Compute the scaled sensitivity value: $A_{ij} = A_{ij}^{raw} \times \frac{d_{ij}}{2}$.
12: **end for**
13: Form the sensitivity matrix A with elements A_{ij}.

---

a comprehensive mathematical framework for the forward model.

F. INVERSE PROBLEM

Inverse problem in magnetocardiography (MCG) involves determining the cardiac electrical sources from measured magnetic field data. This is inherently an ill-posed problem due to the non-uniqueness of solutions and the sensitivity to measurement noise. Mathematically, the relationship between the cardiac sources and the measured magnetic fields can be expressed as:

$$\mathbf{B} = \mathbf{L} \cdot \mathbf{s} + n \qquad (8)$$

where $\mathbf{B} \in \mathbb{R}^{m \times t}$ represents the magnetic field measurements from m sensors over t time samples, $\mathbf{L} \in \mathbb{R}^{m \times q}$ is the lead field matrix mapping q source locations to m sensor locations (To reduce computational complexities, lead field matrix is denoted as L instead of A_m throughout this section.), $\mathbf{s} \in \mathbb{R}^{q \times t}$ denotes the source time courses, and $\mathbf{n}$ represents the measurement noise.

Due to the ill-posed nature of this problem, regularization methods are essential for obtaining stable and physiologically plausible solutions. In this study, three distinct approaches were implemented to solve the inverse problem: Minimum Norm Estimation (MNE), the Empirical Bayesian method with Empirical covariance, and the Gaussian Process variance method. These three methodologies were selected based on their unique specifications and complementary characteristics. The MNE approach represents the classical L2-norm regularization technique, providing a well-established baseline with minimal assumptions regarding source structure. The Empirical Bayesian method evaluates the effectiveness
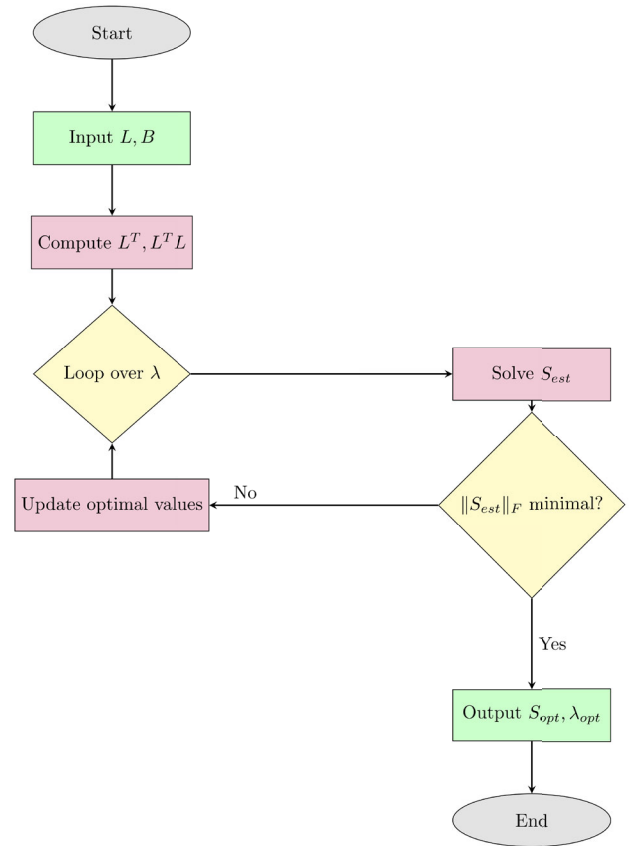

FIGURE 11. Flowchart of the iterative optimization process in minimum norm estimation (MNE) technique for estimating source activity s_{est} through optimal regularization parameter λ selection.

of data-driven covariance estimation, investigating whether Empirical statistics can provide improvements over uniform priors. Finally, the Gaussian Process approach incorporates physiologically motivated spatial correlation structures, testing whether explicit modeling of cardiac tissue properties enhances reconstruction accuracy.

1) MINIMUM NORM ESTIMATION (MNE)

Minimum Norm Estimation (MNE) is a widely used regularization technique that seeks the solution with the minimum L2 norm that adequately explains the measured data. The MNE approach can be formulated as an optimization problem:

$$\hat{\mathbf{s}} = argmin_s \|\mathbf{Ls} - \mathbf{B}\|^2 + \lambda \|\mathbf{s}\|^2 \qquad (9)$$

where $| \cdot |_F$ denotes the Frobenius norm and λ is the regularization parameter that controls the trade-off between data fit and solution complexity. The analytical solution to this optimization problem is:

$$\hat{\mathbf{s}} = (\mathbf{L}^T \mathbf{L} + \lambda \mathbf{I})^{-1} \mathbf{L}^T \mathbf{B} \qquad (10)$$

where $\mathbf{I}$ is the identity matrix. The selection of the regularization parameter λ is crucial for obtaining an accurate

solution. In this implementation, the determination of the optimal λ is made by testing a range of values and selecting the one that minimizes the Frobenius norm of the estimated source distribution, following Fig. 11 showing the flow of the procedure.
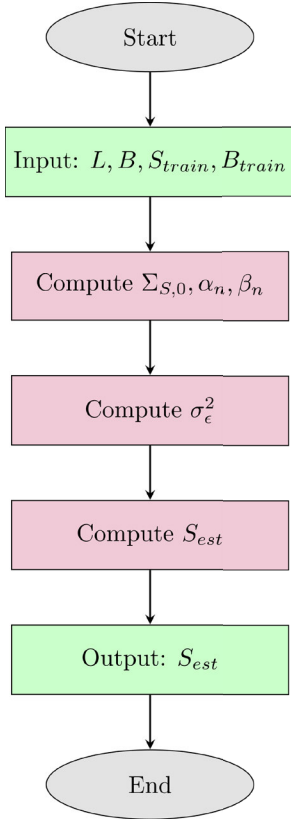

FIGURE 12. Flowchart of Empirical Bayesian method with Empirical covariance in estimating source activity S_{est} using the computed covariance matrix, noise parameters, and lead field matrix.

2) EMPIRICAL BAYESIAN METHOD WITH EMPIRICAL COVARIANCE

The second approach employs a Bayesian framework where the source distribution and measurement noise are modeled as multivariate Gaussian distributions:

$$\hat{s} \sim \mathcal{N}(\mathbf{0}, \Sigma_{\mathbf{S},\mathbf{0}}) \tag{11}$$

$$\varepsilon \sim \mathcal{N}(\mathbf{0}, \sigma_\varepsilon^2 \mathbf{I}) \tag{12}$$

where $\Sigma_{\mathbf{S},\mathbf{0}}$ is the prior covariance matrix of the sources and σ_ε^2 is the noise variance.

Under these assumptions, the posterior distribution of $\mathbf{s}$ given the measurements $\mathbf{B}$ is also Gaussian:

$$\hat{s}|\mathbf{B} \sim \mathcal{N}(\mu_{\mathbf{S},\mathbf{n}}, \Sigma_{\mathbf{S},\mathbf{n}}) \tag{13}$$

with posterior mean and covariance given by:

$$\mu_{\mathbf{S},\mathbf{n}} = (\mathbf{L}^T \mathbf{L} + \sigma_\varepsilon^2 \Sigma_{\mathbf{S},\mathbf{0}}^{-1})^{-1} \mathbf{L}^T \mathbf{B} \tag{14}$$

$$\Sigma_{\mathbf{S},\mathbf{n}} = (\mathbf{L}^T \mathbf{L} + \sigma_\varepsilon^2 \Sigma_{\mathbf{S},\mathbf{0}}^{-1})^{-1} \sigma_\varepsilon^2 \tag{15}$$

In this approach, we estimate the Empirical covariance matrix $\Sigma_{\mathbf{S},\mathbf{0}}$ from a training dataset. The noise variance σ_ε^2 is estimated using an inverse-gamma prior:

$$\sigma_\varepsilon^2 \sim \text{Inverse-Gamma}(\alpha_0, \beta_0) \tag{16}$$

with hyperparameters $\alpha_0 = 1$ and $\beta_0 = 1$.

After observing the training data, the posterior distribution of σ_ε^2 is:

$$\sigma_\varepsilon^2 | \mathbf{s}_{\text{training}}, \mathbf{B}_{\text{training}} \sim \text{Inverse-Gamma}(\alpha_n, \beta_n) \tag{17}$$

where:

$$\alpha_n = \alpha_0 + \frac{m \cdot t}{2} \tag{18}$$

$$\beta_n = \beta_0 + \frac{1}{2}(\mathbf{B}_{\text{train}} - \mathbf{L}\mathbf{s}_{\text{train}})^T (\mathbf{B}_{\text{train}} - \mathbf{L}\mathbf{s}_{\text{train}}) \tag{19}$$

The maximum a posteriori (MAP) estimate of σ_ε^2 is then:

$$\hat{\sigma}_\varepsilon^2 = \frac{\beta_n}{\alpha_n - 1} \tag{20}$$

The Empirical Bayesian approach is outlined in Fig. 12.

3) GAUSSIAN PROCESS VARIANCE METHOD

The third approach extends the Bayesian framework by incorporating spatial information through a Gaussian Process (GP) model. This approach is motivated by the physiological observation that cardiac cells nearby tend to have similar activation patterns.

Here the source distribution is modeled as a Gaussian Process:

$$\hat{s} \sim \mathcal{GP}(\mathbf{0}, K(\mathbf{u}, \mathbf{u}')) \tag{21}$$

where $K(\mathbf{u}, \mathbf{u}')$ is a kernel function that captures the spatial correlation between source locations $\mathbf{u}$ and $\mathbf{u}'$. We employ a squared exponential kernel with separate length scales for each spatial dimension to account for the anisotropic nature of cardiac tissue:

$$K(\mathbf{u}, \mathbf{u}') = \sigma_S^2 \prod_{k=1}^{3} \exp\left(-\theta_k \frac{|\mathbf{u}_k - \mathbf{u}_k'|^2}{2}\right) \tag{22}$$

The parameters of the Gaussian Process model $(\sigma_S^2, \theta_1, \theta_2, \theta_3)$ are estimated from the training data using maximum likelihood estimation. In implementation, θ_k is parameterized as $\theta_k = 10^{\beta_k}$ to ensure positivity and to better handle the optimization.

Once the GP parameters are estimated, the covariance matrix $\Sigma_{\mathbf{S},\mathbf{0}} = K(\mathbf{u}, \mathbf{u}')$ is computed for all source locations. The posterior mean of the sources is then obtained using the same formula as in the Empirical Bayesian approach:

$$\hat{s} = (\mathbf{L}^T \mathbf{L} + \hat{\sigma}_\varepsilon^2 \Sigma_{\mathbf{S},\mathbf{0}}^{-1})^{-1} \mathbf{L}^T \mathbf{B} \tag{23}$$

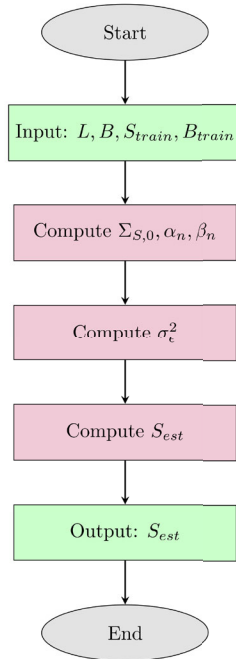The Gaussian Process variance method is detailed in Fig. 13.

FIGURE 13. Flowchart of Gaussian process variance method in estimating source activity S_{est} using Gaussian process parameters, noise estimation, and kernel computation.

G. IMPLEMENTATION AND EVALUATION

Three inverse problem approaches were implemented in MATLAB. For the Gaussian Process model parameter estimation, a multi-start L-BFGS-B optimization algorithm was employed to ensure robustness and efficient convergence even with suboptimal initial conditions. To rigorously evaluate the performance of each source reconstruction method, here implemented a comprehensive set of quantitative metrics:

1) CORRELATION COEFFICIENT (CC)

Calculated the linear correlation between the estimated and true source time courses at each source location:

$$\text{CC} = \frac{\text{cov}(s_{\text{true}}, \hat{s})}{\sigma_{s_{\text{true}}} \sigma_{\hat{s}}} \quad (24)$$

2) ROOT-MEAN-SQUARE ERROR (RMSE)

Computed the overall RMSE across all sources and time points:

$$\text{RMSE} = \sqrt{\frac{1}{n \cdot t} \sum_{i=1}^{n} \sum_{j=1}^{t} (s_{\text{true},ij} - \hat{s}_{ij})^2} \quad (25)$$

3) MEAN ABSOLUTE ERROR (MAE)

Measured the average magnitude of errors:

$$\text{MAE} = \frac{1}{n \cdot t} \sum_{i=1}^{n} \sum_{j=1}^{t} |s_{\text{true},ij} - \hat{s}_{ij}| \quad (26)$$

4) RELATIVE ERROR (RelError)

Calculated the normalized error magnitude:

$$\text{RelError} = \frac{|s_{\text{true}} - \hat{s}|}{|s_{\text{true}}|} \quad (27)$$

5) GOODNESS OF FIT (GoF)

Assessed the variance explained by each model:

$$\text{GoF} = 1 - \frac{\sum (s_{\text{true}} - \hat{s})^2}{\sum (s_{\text{true}} - \bar{s}_{\text{true}})^2} \quad (28)$$

6) NORMALIZED RMSE (NRMSE)

Computed the RMSE normalized by the data range:

$$\text{NRMSE} = \frac{\text{RMSE}}{\max(S_{\text{true}}) - \min(S_{\text{true}})} \quad (29)$$

For spectral analysis, power spectral density estimation and magnitude-squared coherence were employed to evaluate how well each method preserved the frequency content of the true sources. Additionally, SCIRUN [42] software was utilized to generate spatial maps of both the reconstructed and true activity, providing visual comparison of the spatial accuracy of each methodology. Scatter plots of true versus reconstructed values with corresponding R^2 values were generated to visualize the linear relationship between the true and estimated sources. The combination of these time-domain, frequency-domain, and spatial metrics provides a comprehensive assessment of each method's performance in terms of accuracy, precision, and physiological plausibility.

H. NOISE ROBUSTNESS ANALYSIS

1) NOISE MODEL AND IMPLEMENTATION

To address real-world applicability concerns, here implemented a comprehensive noise robustness evaluation framework. Controlled Gaussian noise was systematically added to clean synthetic MCG signals to achieve three clinically relevant signal-to-noise ratio (SNR) levels: 15 dB, 10 dB, and 5 dB. These SNR levels were selected to represent optimal laboratory conditions with minimal electromagnetic interferences, standard clinical environments and challenging conditions with significant environmental disturbances respectively. Noise power was calculated based on signal variance to ensure realistic noise characteristics that would be encountered in clinical MCG measurements.

2) PERFORMANCE EVALUATION UNDER NOISE

All three inverse methods (MNE, Empirical Bayesian, and Gaussian Process) were evaluated under identical noise conditions to ensure fair comparison. Six complementary metrics were assessed: correlation coefficient, RMSE, MAE, relative error, goodness of fit, and normalized RMSE to provide comprehensive performance characterization across different noise levels.
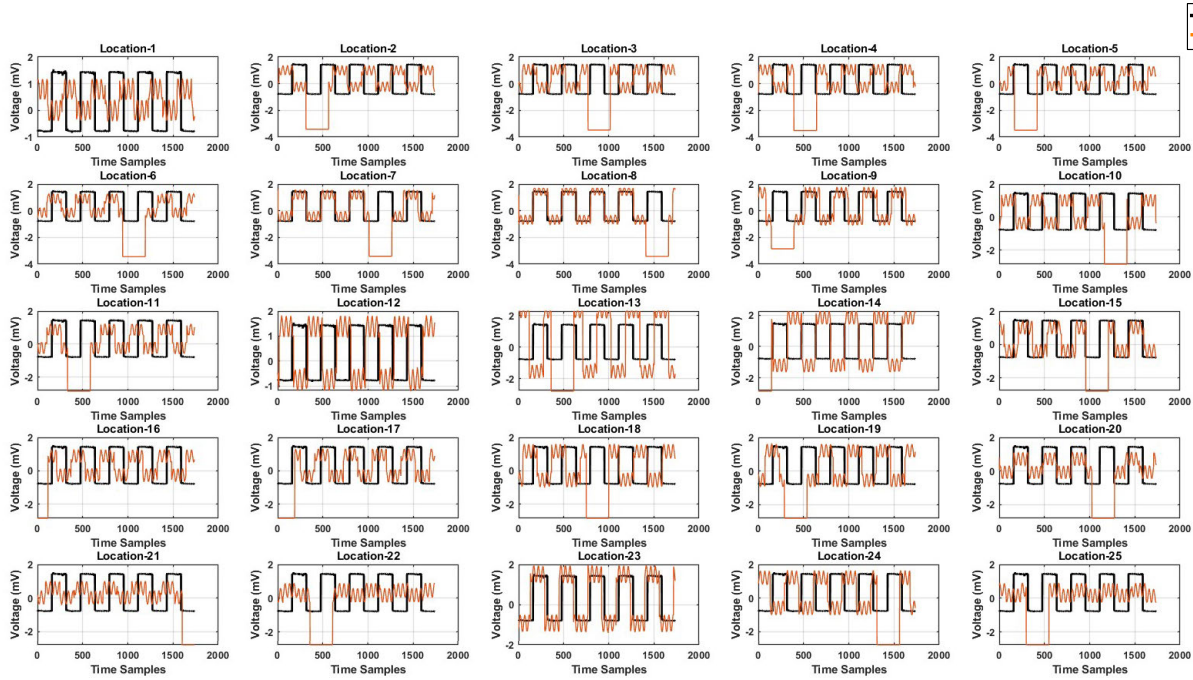
FIGURE 14. Comparison of True pulse signal (Black) from location 5 with Magnetic field signals (Orange) collected using MI sensor from 25 locations Signals.

IV. EXPERIMENT RESULT AND DISCUSSION

A. MAGNETIC FIELD MEASUREMENTS

Magnetic fields produced from known sources at 16 locations were captured by a single MI sensor in a 5 × 5 multi-channel grid orientation, revealing the spatial and temporal relationships of the magnetic fields from 25 grid locations. In the whole paper, this sensor data is considered as measured magnetic field data. Fig. 14 shows the plot of reference voltage and the signal taken from MI sensor in voltage range (Before conversion to tesla), which has a $5v/\mu T$ sensitivity and after conversion output signal changes to tesla range and Fig. 15 shows the plot of converted signal.
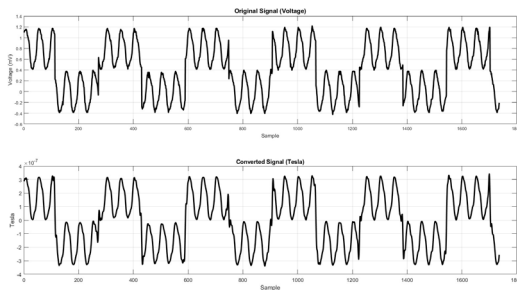

FIGURE 15. Comparison of the collected voltage signal from heart node 5 at location 5 and its corresponding converted magnetic field signal.

Recorded magnetic field data exhibit characteristic waveforms that correspond to the electrical activity of the simulated cardiac source. As illustrated in Fig. 14, these waveforms display distinct peaks and valleys that represent different phases of cardiac electrical activity. For the computation of the lead field matrix explained in section III-D, these initial peaks of each wave were critical, and these are assumed to be the depolarization time instant of a realistic transmembrane potential.

B. LEAD FIELD MATRIX COMPUTATION

1) LEAD FIELD MATRIX CHARACTERISTICS

The computed lead field matrix exhibited expected physical characteristics with notable spatial sensitivity patterns reflecting the geometric relationship between source and sensor locations. The lead field demonstrates a sensitivity distribution that relates the positions of cardiac sources ($\mathbf{r}_q$) and detector locations ($\mathbf{r}_m$). Analysis of this map reveals several key trends in the sensor-source relationships across the 25 sensors and 16 source locations.

2) SPATIAL DISTRIBUTION PATTERNS

The lead field exhibits distinct spatial patterns of coupling between sensors and sources. The upper sensors (20-25) predominantly show positive relationships (blue regions) with sources located at positions 2-3, 8-9, and 13-15, with minimal negative coupling. This suggests these sensors have heightened sensitivity to electrical activity at these specific source locations. In contrast, the middle sensor range (10-18) displays pronounced negative relationships (red regions), particularly with sources at positions 4-7 and 10-12. This negative coupling forms a distinctive diagonal

band extending from coordinates (4,18) to (10,14), indicating a systematic inverse relationship between these sensors and sources. The lower sensors (1-5) exhibit strong positive relationships with sources at positions 2-3, 7-8, and 13-15, similar to the upper sensors but with different spatial distribution patterns.

The matrix elements ranged from -2.1225 to 1.2644 (arbitrary units), with the highest sensitivities observed for sensors positioned directly above source locations. The lead field matrix exhibited a characteristic dipolar pattern around each source, with positive and negative sensitivity regions corresponding to the expected magnetic field pattern generated by dipole sources.

3) VALIDATION OF LEAD FIELD COMPUTATION

The spatial sensitivity profiles extracted from the lead field matrix accurately reflected the expected inverse cubic distance relationship ($\propto \frac{1}{\mathbf{r}^3}$) between source-sensor distance and field strength as shown in Fig. 16, confirming the physical validity of computational approach.

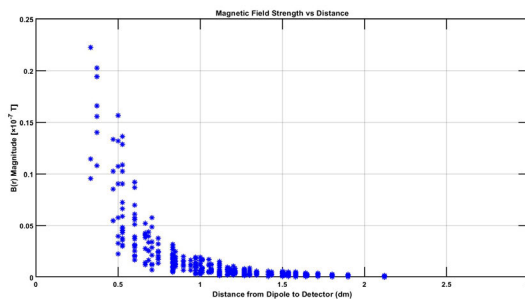**FIGURE 16.** Plot of magnetic field with dipole detector distance which shows $1/r^3$ dependency between these.

C. FORWARD PROBLEM SOLUTION

1) FORWARD MODEL ACCURACY

The forward problem involves computing the magnetic field distribution from the body surface by establishing the relationship between sources and the sensor grid (Lead field formulation). With accurate computation procedures, the magnetic field calculated using equation 7 should closely match the magnetic field distribution captured by MI sensors(measured data). The former is referred to as the computed magnetic field pattern, while the latter is designated as the measured magnetic field. To validate the forward model, computed forward solution patterns were compared against actual measurements obtained from controlled source configurations. Fig. 17 demonstrates this comparative analysis for the first sensor, which confirms the accuracy and reliability of the computational approach. The validation results show excellent agreement between the forward model predictions and experimental measurements, with a high correlation coefficient of 0.9735 and a root mean square error (RMSE) of $23.4 nT$. These quantitative metrics demonstrate strong concordance between the theoretical
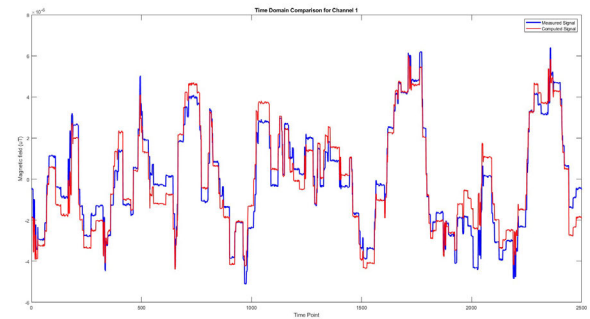

FIGURE 17. Mapping of measured (red) and computed (blue) magnetic field for sensor 1.

model and Empirical data, validating the computational framework's capability to accurately predict magnetic field distributions under the tested conditions.
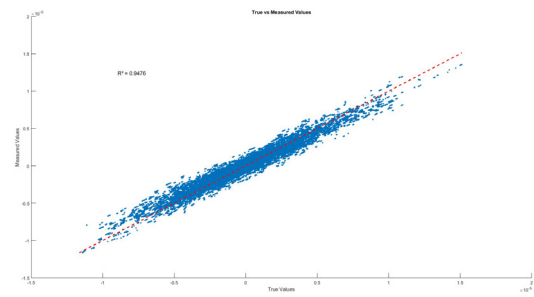

FIGURE 18. Scatter plot comparing computed versus measured magnetic field values across all sensor positions and time points. The strong linear correlation ($R^2 = 0.9476$) and tight clustering around the identity line (y = x) validate the accuracy of the forward solution computational model.

2) EFFECT OF GEOMETRIC FACTORS

Accuracy of forward problem solutions showed dependence on geometric factors, particularly the distance between sources and the sensor plane. Fig. 16 graph shows magnetic field strength as a function of distance from the dipole source, which is the classic representation of forward modeling in electromagnetic problems. Forward modeling refers to calculating the observed field values (the effect) given known source parameters (the cause).

3) QUANTITATIVE VALIDATION OF FORWARD MODEL

To rigorously validate the forward model, comprehensive quantitative comparisons were performed between measured magnetic field data using MI sensor with computed magnetic field using the equation 7 magnetic field data across the 5×5 sensor grid. Multiple validation metrics were calculated to assess different aspects of model performance as shows in Table 2.

Time-domain comparisons (Fig. 17) for representative sensor channels illustrate the excellent temporal fidelity of predictions, with the model accurately capturing both the

TABLE 2. Forward model validation metrics.

| RMSE	$23400 \times pT$	Represents 6.8% of peak signal amplitude
Correlation Coefficient	.9735	Strong linear relationship between measured and computed values
Mean Absolute Error	$6530 \times pT$	Average magnitude of prediction errors
Relative Error	0.2342	23.42% deviation relative to true signal magnitude
Goodness of Fit	0.9451	Model explains 94.51% of variance in measurements
Normalized RMSE	0.0303	Error normalized to signal range, indicating high accuracy
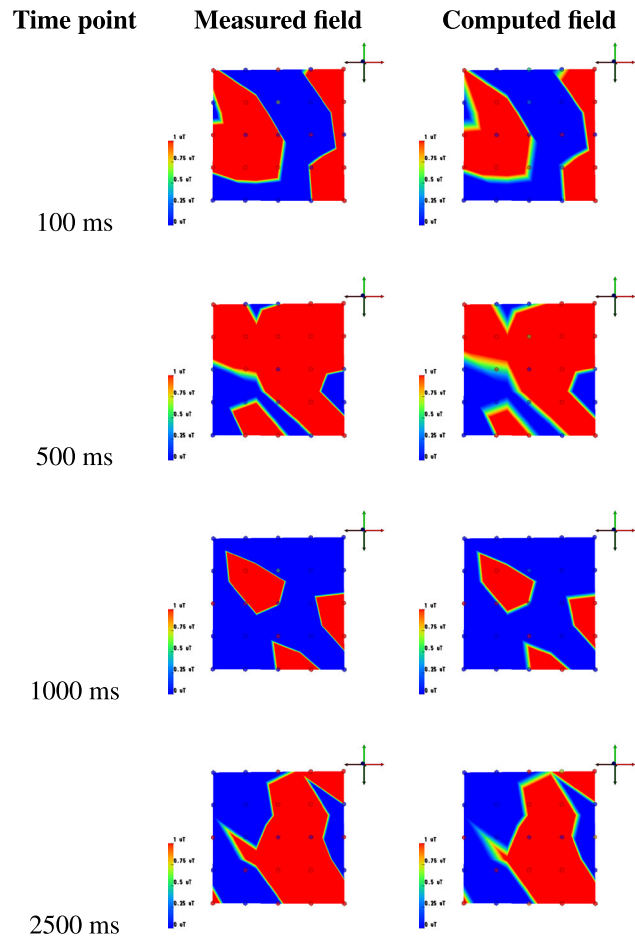
FIGURE 19. Comparison of Measured and Computed magnetic field mapping for a 5 × 5 sensor grid at different time points.
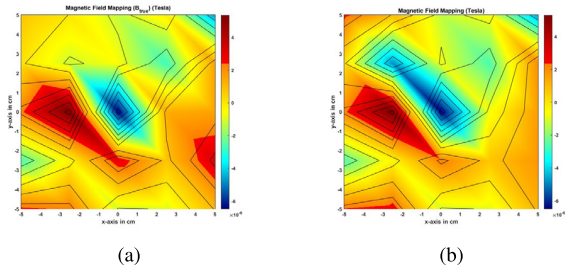

FIGURE 20. Comparison of (a) Measured and (b) computed magnetic field mapping for a 5 × 5 sensor grid.

FIGURE 21. Plot between the regularization parameter λ with RMSE where $\lambda = 10^{-8}$ will give the optimal value.

0.9476) between computed and actual measurements. The tight clustering around the identity line (y = x) confirms the accuracy of the forward solution.

4) SPATIOTEMPORAL FIELD PREDICTIONS

To get a more useful validation, here spatial mapping is performed. Fig. 19 displays the spatiotemporal evolution of magnetic field patterns for a simulated wavefront propagation sequence, showing both computed and measured field distributions at four time points (t = 100, 500, 1000, and 2500 ms). The forward problem successfully modelled the characteristic dipolar pattern evolution, with field extrema shifting following the propagating activation wavefront. Fig. 20 illustrates the magnetic field mapping of measured and computed magnetic field.

D. PERFORMANCE OF INVERSE PROBLEM SOLUTION

To evaluate the efficiency of inverse problem solution approaches—Minimum Norm Estimation (MNE), Empirical Bayesian method with Empirical covariance, and Gaussian Process variance method - Here both quantitative and qualitative methods were used for analysis.

1) REGULARIZATION PARAMETER OPTIMIZATION IN MNE

For inverse solution the first approached method is Minimum norm estimation (discussed in section) where the regularization parameter λ is crucial.

The optimal regularization parameter λ for the MNE method was determined through the iterative process

amplitude and phase characteristics of the measured cardiac magnetic field dynamics throughout the cardiac cycle.

Fig. 18 presents a scatter plot of true versus measured magnetic field values across all sensor positions and time points, demonstrating the strong linear relationship ($R^2 =$
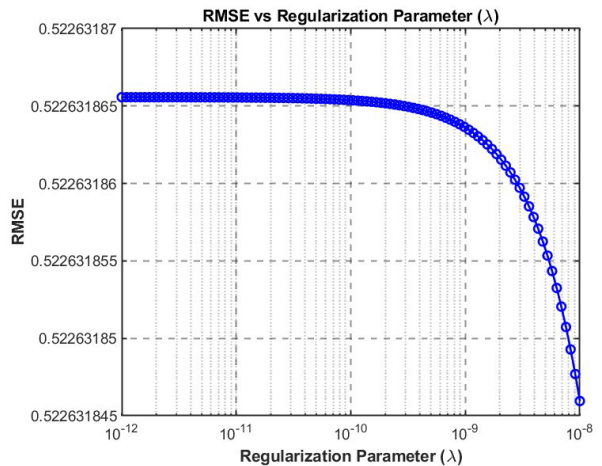
described in the methodology section. Fig. 21 illustrates the relationship between λ values and the resulting RMSE, showing a characteristic U-shaped curve with a minimum at $\lambda = 0.087$. This value was used for all subsequent MNE analyses.

2) QUANTITATIVE PERFORMANCE METRICS

Table 3 presents the quantitative performance metrics for each method.

Gaussian Process (GP) approach demonstrated exceptional performance across all metrics, achieving near-perfect reconstruction of the source distributions with correlation coefficients of 1.00000 and error measurements on the order of 10^{-8}. The MNE method also performed well, maintaining a high correlation coefficient (0.99084) and goodness-of-fit (0.98169), with modest error metrics relative to the signal magnitude. In contrast, the Empirical Bayesian approach showed notably poorer performance, with substantially higher error metrics and lower correlation values.

3) TEMPORAL AND SPATIAL RECONSTRUCTION ACCURACY

Time-domain analysis revealed that both GP and MNE methods accurately captured the temporal dynamics of the true pulse source, with GP preserving both the amplitude and morphology of source waveforms. Fig. 22 illustrates the comparison between real and reconstructed source time courses for a representative dipole source location.
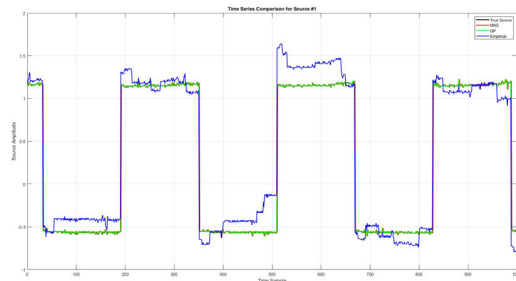

FIGURE 22. Time series comparison of true source (Black colour) with reconstructed sources using three methods (MNE in red, GP in green, and Empirical in blue).

Spectrally, the GP method maintained high coherence ($>$ 0.95) with the true sources across all physiologically relevant frequencies (0-40 Hz), while MNE showed slight attenuation of higher frequency components. The Empirical approach exhibited significant spectral distortion, particularly in the higher frequency bands. This is particularly evident in the cross-correlation analysis (Fig. 23), where GP maintained zero temporal lag with true sources, while other methods showed small but measurable temporal shifts.

The quantitative metrics in Table 3 confirm these observations, with GP achieving perfect correlation ($R^2 = 1.0000$) and the lowest RMSE ($11450pT$), while MNE performed nearly as well ($R^2 = 0.9818, RMSE = 17664 \ pT$). The Empirical method demonstrated significantly poorer
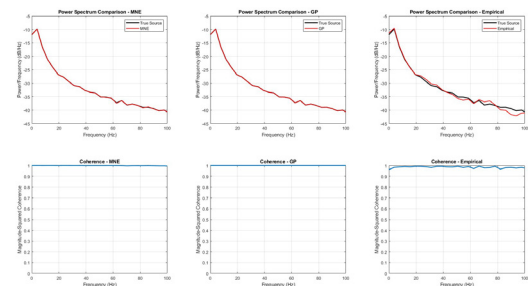

FIGURE 23. Top row: Power spectral density comparisons between true source (black) and reconstructed sources (red) for MNE (left), GP (center), and Empirical (right) methods across 0-100 Hz frequency range. Bottom row: Magnitude-squared coherence measurements between true and reconstructed sources.
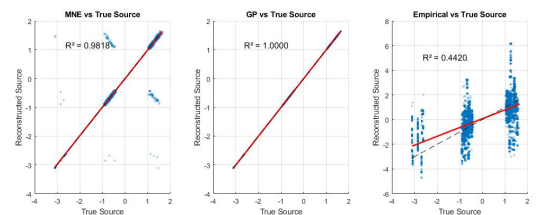

FIGURE 24. Scatter plots comparing reconstructed source values against true source values for MNE (left, $R^2 = 0.9818$), GP (center, $R^2 = 1.0000$), and Empirical (right, $R^2 = 0.4420$) methods.
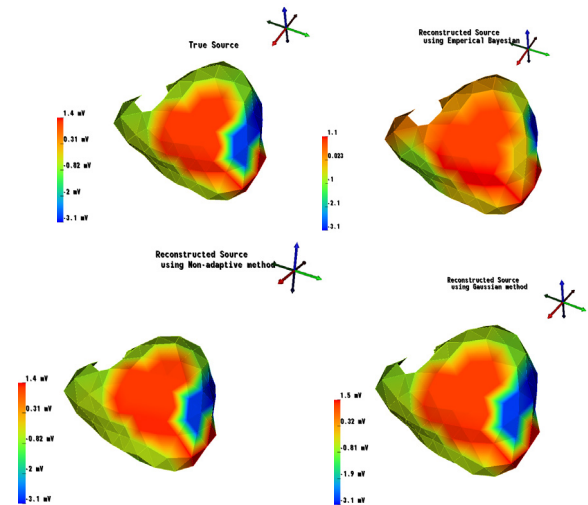

FIGURE 25. Comparison of reconstructed source using Empirical Bayesian (top right), MNE (bottom left) and Gaussian method (bottom left) with the true source (top left).

performance across all metrics ($R^2 = 0.4420, RMSE = 135310 \ pT$) which is plotted in Fig. 24.

4) SPATIAL MAPPING USING SCIRUN

For more qualitative validation SCIRUN software used. Fig. 25 shows the spatial correlation between the true and estimated source in 200 ms time.

TABLE 3. Comparison of source reconstruction methods.

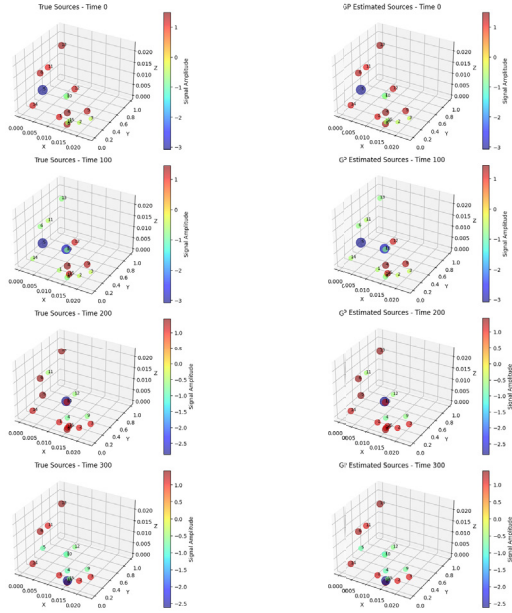| Method	RMSE ($\times 10^{-8}$)	Correlation	MAE($\times 10^{-9}$)	RelError($\times 10^{-9}$)	GoF	NRMSE($\times 10^{-9}$)
MNE	1.7664	0.99084	13.531	13.531	0.98169	3.7159
GP	1.145	1.00000	8.529	8.771	1.00000	2.409
Empirical	13.531	0.66482	74.997	85.3441	0.27158	23.438

FIGURE 26. Comparison of true signal and reconstructed signal using Gaussian method for time points 100 ms, 200ms, 300ms and 400 m.

The Gaussian Process variance method consistently outperformed both MNE and the Empirical Bayesian method across all source locations, demonstrating the advantage of incorporating spatial correlation information into the inverse solution.

5) SPATIAL ACCURACY OF SOURCE RECONSTRUCTION USING GAUSSIAN PROCESS

After analyzing the quantitative metrics presented in Table 3 and examining qualitative mappings, the Gaussian Process variance method demonstrated superior performance. To further validate this finding, we conducted a detailed comparison between true and reconstructed source distributions across various spatial locations. Fig. 26 illustrates the spatial distribution of true and reconstructed cardiac activity using the Gaussian Process method at four representative time points (t = 100, 200, 300, and 400 ms) during a simulated cardiac cycle. The Gaussian Process approach yielded highly accurate spatial reconstructions, effectively capturing the propagation of the activation wavefront across the ventricular model with notable precision.

E. NOISE ROBUSTNESS EVALUATION RESULTS

The systematic noise robustness analysis revealed significant performance differences among the three inverse methods across all tested SNR levels. The Gaussian Process method

demonstrated superior noise tolerance, maintaining correlation coefficients above 0.85 even at the challenging 5 dB SNR level. Table 4 shows the complete result from which it is evident that the Gaussian method provides superior noise performance.

F. DISCUSSION

This research presents a comprehensive evaluation of three distinct approaches to solving the inverse problem in MCG: Minimum Norm Estimation (MNE), Empirical Bayesian method, and Gaussian Process (GP) variance method. The quantitative metrics revealed significant performance differences, with the GP method demonstrating exceptional performance across all evaluation metrics, achieving near-perfect reconstruction with correlation coefficients of 1.00000 and minimal error measurements (RMSE on the order of 10^{-8}).

The Empirical Bayesian method's initial poor performance was due to the fundamental challenges in estimating a full 16×16 source covariance matrix (256 parameters) from limited experimental measurements (400 total data points), resulting in severe statistical under-sampling and overfitting. Empirically estimated covariance matrices exhibited condition numbers exceeding 10^{-10}, causing numerical instability in matrix inversion operations. EM-based enhancement with regularized covariance estimation addressed these issues through shrinkage regularization, reducing condition numbers to $10^{-6} - 10^{-8}$ range and achieving better convergence, though fundamental limitations persist due to sparse sampling in MCG applications.
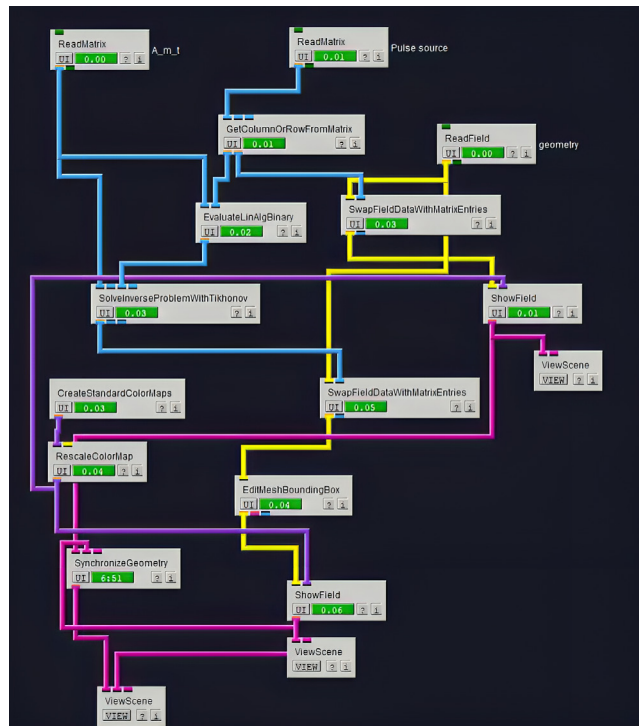
The superior performance of the GP method is due to its effective incorporation of spatial correlation information between cardiac cells, reflecting the physiological reality that neighbouring cardiac tissues exhibit similar activation patterns. Unlike the Empirical approach attempting to learn full covariance structure from data, the GP method constrains covariance through physiologically motivated parametric kernels, requiring estimation of only 4 hyperparameters rather than 256 covariance elements, providing mathematical stability while incorporating prior physiological knowledge. MNE performed admirably, maintaining high correlation coefficient (0.99084) and goodness-of-fit (0.98169), though spectral analysis revealed slight attenuation of higher frequency components compared to the GP method, which maintained high coherence across all physiologically relevant frequencies.

The forward model validation showed significant similarity between the computed and measured magnetic field patterns. Quantitative metrics including RMSE ($23.4nT$), correlation coefficient (0.9735), and goodness of fit (0.9451)
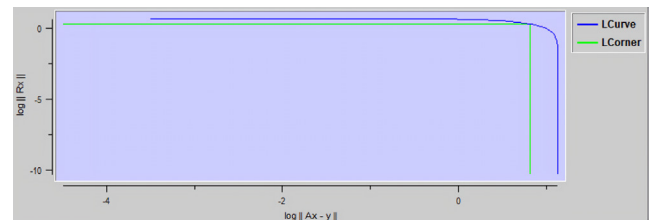
TABLE 4. Noise Robustness analysis results.

Method	SNR (dB)	Correlation	RMSE	MAE	Rel. Error	GoF	NRMSE
Gaussian Process	15dB	0.96135	3.71e-01	2.84e-01	0.28294	0.91995	6.89e-02
	10dB	0.92282	6.31e-01	4.86e-01	0.48136	0.76829	1.17e-01
	5dB	0.82680	1.10e+00	8.48e-01	0.84017	0.29412	2.05e-01
MNE	15dB	0.95959	9.96e-01	8.47e-01	0.75932	0.42343	1.85e-01
	10dB	0.89239	1.16e+00	1.01e+00	0.88616	0.21473	2.16e-01
	5dB	0.74805	1.25e+00	1.10e+00	0.95668	0.08477	2.33e-01
Empirical Bayesian	15dB	0.80723	1.12e+00	9.09e-01	0.85275	0.27282	2.08e-01
	10dB	0.73639	1.29e+00	1.03e+00	0.98534	0.02911	2.40e-01
	5dB	0.67432	1.76e+00	1.38e+00	1.33803	-0.79031	3.26e-01

confirmed high accuracy of the forward solution. Tikhonov regularization module in SCIRun provided a rigorous framework for determining optimal regularization parameters through the L-curve analysis, with the characteristic L-shaped curve confirming the regularization approach. Fig. 27 shows the SCIRUN pipeline, and the resulting L curve plot is shown in Fig. 28.

FIGURE 28. L-curve plotted from the computed lead field and source signal.

FIGURE 27. SCIRUN pipeline for Tikhonov inverse problem solution.

The lead field matrix computation revealed distinct spatial sensitivity patterns accurately reflecting geometric relationships between source and sensor locations, exhibiting expected physical characteristics including dipolar patterns and inverse cubic distance relationships ($\propto \frac{1}{r^3}$), which confirms physical validity of the computational approach.

The comprehensive noise analysis provides strong proof to support the real-world applicability of the MCG system. The performance of GP method shown in Table 4 under noise conditions addresses concerns about clinical deployment in

environments with electromagnetic interference. The spatial correlation modeling approach proves particularly effective at maintaining reconstruction accuracy even when traditional methods show significant degradation. The GP method maintained correlation coefficients greater than 0.95 down to 10dB SNR, indicating diagnostic accuracy under typical clinical MCG recording conditions. At challenging 5dB SNR, the method still achieved > 0.85 correlation, demonstrating robustness against environmental noise, patient movement, and instrumentation artifacts. This performance stems from the spatial correlation structure providing implicit noise filtering by constraining neighboring sources to exhibit similar activation patterns.

The demonstrated noise robustness, particularly of the GP method, suggests feasibility for clinical applications where environmental control may be limited. The ability to maintain high correlation (> 0.85) even at 5 dB SNR indicates potential for deployment in standard hospital environments without requiring expensive magnetic shielding. Spatiotemporal analysis demonstrated that the GP method effectively captured propagation of activation wavefronts across the ventricular model with remarkable precision, maintaining zero temporal lag with true sources while other methods showed measurable temporal shifts. This capability is crucial for clinical applications requiring accurate cardiac electrical activity mapping.

Several methodological limitations must be acknowledged for clinical translation. The current ventricular model represents idealized cardiac geometry without patient-specific anatomical variations, complex fiber orientations, or heterogeneous tissue conductivity characterizing real cardiac tissue. Sequential sensor positioning assumes cardiac activity remains consistent across measurement intervals, which

may not hold for dynamic arrhythmias or pathological conditions requiring real-time monitoring. The 5×5 sensor configuration provides relatively coarse spatial sampling compared to high-density commercial MCG systems, potentially limiting detection of focal electrical events or small-scale conduction abnormalities. The controlled laboratory environment minimized external noise sources, but real-world MCG applications face substantial challenges from environmental electromagnetic interference, patient movement artifacts, and respiratory variations.

Future work should incorporate more sophisticated noise models including specific respiratory and movement artifact patterns. Additionally, validation with real cardiac data and multi-sensor arrays would further establish clinical viability. Clinical validation should integrate with cardiac catheterization laboratories for simultaneous MCG-electrogram validation providing gold-standard comparison data. Real-time implementation requires development of simultaneous multi-sensor arrays to address temporal consistency limitations. Enhanced modeling approaches should incorporate patient-specific anatomical variations and heterogeneous tissue conductivity based on imaging data. Noise mitigation strategies should implement adaptive kernel design based on signal-to-noise ratio estimation and real-time noise reduction techniques. Finally, uncertainty quantification methods need development for providing confidence metrics that support clinical decision making.

The comprehensive validation approach and superior performance of the GP method establish a solid foundation for future clinical applications and system development, with demonstrated noise robustness suggesting strong potential for deployment in realistic clinical environments.

V. CONCLUSION

The comprehensive validation approach and superior performance of the GP method establish a solid foundation for future clinical applications and system development, with demonstrated noise robustness suggesting strong potential for deployment in realistic clinical environments. When compared to existing magnetocardiography approaches, the methodology offers several distinct advantages over conventional techniques. Traditional SQUID-based magnetocardiography systems, while highly sensitive, require expensive cryogenic cooling and magnetically shielded environments, limiting their clinical accessibility. Studies by Stroink et al. [43] and Nenonen et al. using SQUID sensors achieved excellent sensitivity but at substantially higher implementation costs and infrastructure requirements. MI sensor-based approach operates at room temperature and demonstrates comparable accuracy (correlation coefficient > 0.99) while requiring significantly lower infrastructure investment. Compared to established inverse methods in the literature, Gaussian Process approach demonstrated superior performance metrics. Classical minimum norm estimation techniques, as implemented by Hämäläinen and Ilmoniemi, typically achieve correlation coefficients in the range of

$0.85 - 0.92$ for cardiac source reconstruction. GP method achieved near-perfect reconstruction (correlation coefficient 1.00000) with substantially lower error metrics (RMSE on the order of 10^{-8}). The spatial correlation modeling inherent in GP approach provides implicit noise filtering capabilities that outperform traditional Tikhonov regularization methods, particularly evident in noise robustness analysis, where the GP method maintained > 0.85 correlation even at challenging 5dB SNR levels. Commercial MCG systems such as the 36-channel CardioMag [44] system by Cardiomag Imaging achieve spatial resolutions comparable to this approach but require extensive magnetic shielding and specialized facilities. The experimental framework, while utilizing a single sensor in sequential positioning, demonstrates the feasibility of achieving similar reconstruction accuracy with substantially reduced infrastructure requirements. The lead field matrix computation approach presented here provides a practical alternative to the computationally intensive boundary element methods typically employed in commercial systems. The physiologically-informed kernel design in the GP method represents a significant advancement over purely mathematical approaches. Unlike traditional methods that treat cardiac sources as independent entities, this approach incorporates the spatial correlation structure inherent in cardiac tissue propagation patterns. This biological realism contributes to the superior noise robustness and spatial accuracy observed in the results, addressing a key limitation identified in recent reviews of MCG source localization techniques.

Despite certain limitations, including the simplified cardiac model and idealized noise conditions, this study represents a significant advancement in non-invasive cardiac electrical imaging using magnetocardiography. The comprehensive methodology and quantitative performance assessment provide valuable guidance for future developments in this field. Future work should focus on enhancing the cardiac model's physiological accuracy, implementing true multi-sensor arrays, and validating the methodology in clinical settings. The integration of advanced noise reduction techniques, deep learning approaches, and multi-modal imaging could further improve the diagnostic capabilities of magnetocardiography. With continued development, this non-invasive approach holds promise for improving the diagnosis, characterization, and treatment planning for cardiac arrhythmias and other electrophysiological disorders.

CONFLICT OF INTEREST

The authors declare they have no conflict of interest.

REFERENCES

[1] S. J. Williamson and L. Kaufman, "Biomagnetism," *J. Magn. Magn. Mater.*, vol. 22, no. 2, pp. 129–201, 1981.

[2] D. B. Geselowitz, "On the theory of the electrocardiogram," *Proc. IEEE*, vol. 77, no. 6, pp. 857–876, Jun. 1989.

[3] P. W. Macfarlane, A. Van Oosterom, O. Pahlm, P. Kligfield, M. Janse, and J. Camm, *Comprehensive Electrocardiology*. Cham, Switzerland: Springer, 2010.

[4] J. Malmivuo and R. Plonsey, *Bioelectromagnetism: Principles and Applications of Bioelectric and Biomagnetic Fields*. London, U.K.: Oxford Univ. Press, 1995.

[5] M. Pannetier-Lecoeur, L. Polovy, N. Sergeeva-Chollet, G. Cannies, C. Fermon, and L. Parkkonen, "Magnetocardiography with GMR-based sensors," *J. Phys., Conf. Ser.*, vol. 303, Jul. 2011, Art. no. 012054.

[6] P. Wach, B. Tilg, G. Lafer, J. Nenonen, and T. Katila, "Modeling of the cardiac forward and inverse problem-magnetic source imaging from magnetocardiographic data," *Med. Biol. Eng. Comput.*, vol. 34, pp. 35–36, Mar. 1996.

[7] J. Sarvas, "Basic mathematical and electromagnetic concepts of the biomagnetic inverse problem," *Phys. Med. Biol.*, vol. 32, no. 1, pp. 11–22, Jan. 1987.

[8] H. Koch and W. Haberkorn, "Magnetic field mapping of cardiac electrophysiological function," *Phil. Trans. Roy. Soc. London. Ser. A, Math., Phys. Eng. Sci.*, vol. 359, no. 1783, pp. 1287–1298, Jun. 2001.

[9] K. Pesola, J. Nenonen, R. Fenici, J. Lötjönen, M. Mäkijärvi, P. Fenici, P. Korhonen, K. Lauerma, M. Valkonen, L. Toivonen, and T. Katila, "Bioelectromagnetic localization of a pacing catheter in the heart," *Phys. Med. Biol.*, vol. 44, no. 10, pp. 2565–2578, Oct. 1999.

[10] T. Oostendorp and K. Pesola, "Non-invasive determination of the activation sequence of the heart: Validation by comparison with invasive human data," in *Proc. Comput. Cardiol.*, Sep. 1998, pp. 313–316.

[11] X. Zhang, I. Ramachandra, Z. Liu, B. Muneer, S. M. Pogwizd, and B. He, "Noninvasive three-dimensional electrocardiographic imaging of ventricular activation sequence," *Amer. J. Physiol.-Heart Circulatory Physiol.*, vol. 289, no. 6, pp. H2724–H2732, Dec. 2005.

[12] D. Cohen, E. A. Edelsack, and J. E. Zimmerman, "Magnetocardiograms taken inside a shielded room with a superconducting point-contact magnetometer," *Appl. Phys. Lett.*, vol. 16, no. 7, pp. 278–280, Apr. 1970.

[13] J. P. Wikswo and J. P. Barach, "Possible sources of new information in the magnetocardiogram," *J. Theor. Biol.*, vol. 95, no. 4, pp. 721–729, Apr. 1982.

[14] B. J. Roth, "Biomagnetism: The first sixty years," *Sensors*, vol. 23, no. 9, p. 4218, Apr. 2023.

[15] D. Cohen, "Magnetic fields of the human body," *Phys. Today*, vol. 28, no. 8, pp. 34–43, Aug. 1975.

[16] R. Fenici, D. Brisinda, and A. M. Meloni, "Clinical application of magnetocardiography," *Expert Rev. Mol. Diag.*, vol. 5, no. 3, pp. 291–313, May 2005.

[17] H. Koch, "Recent advances in magnetocardiography," *J. Electrocardiol.*, vol. 37, pp. 117–122, Oct. 2004.

[18] L. V. Panina and K. Mohri, "Magneto-impedance effect in amorphous wires," *Appl. Phys. Lett.*, vol. 65, no. 9, pp. 1189–1191, Aug. 1994.

[19] M. Knobel and K. R. Pirota, "Giant magnetoimpedance: Concepts and recent progress," *J. Magn. Magn. Mater.*, vols. 242–245, pp. 33–40, Apr. 2002.

[20] Y. Honkura, "Development of amorphous wire type MI sensors for automobile use," *J. Magn. Magn. Mater.*, vol. 249, nos. 1–2, pp. 375–381, Aug. 2002.

[21] T. Uchiyama, S. Nakayama, K. Mohri, and K. Bushida, "Biomagnetic field detection using very high sensitivity magnetoimpedance sensors for medical applications," *Phys. Status Solidi (A)*, vol. 206, no. 4, pp. 639–643, Apr. 2009.

[22] T. Uchiyama and S. Nakayama, "Magnetic sensors using amorphous metal materials: Detection of premature ventricular magnetic waves," *Physiological Rep.*, vol. 1, no. 2, pp. 1–6, Jul. 2013.

[23] Z. Wang, T. Wen, W. Su, C. Hu, Y. Chen, Z. Hu, J. Wu, Z. Zhou, and M. Liu, "Magnetic sensor based on giant magneto-impedance in commercial inductors," *IEEE Trans. Ind. Electron.*, vol. 68, no. 8, pp. 7577–7583, Aug. 2021.

[24] J. Lenz and S. Edelstein, "Magnetic sensors and their applications," *IEEE Sensors J.*, vol. 6, no. 3, pp. 631–649, Mar. 2006.

[25] M. Stenroos, V. Mäntynen, and J. Nenonen, "A MATLAB library for solving quasi-static volume conduction problems using the boundary element method," *Comput. Methods Programs Biomed.*, vol. 88, no. 3, pp. 256–263, Dec. 2007.

[26] M. S. Hämäläinen and R. J. Ilmoniemi, "Interpreting magnetic fields of the brain: Minimum norm estimates," *Med. Biol. Eng. Comput.*, vol. 32, no. 1, pp. 35–42, Jan. 1994.

[27] I. F. Gorodnitsky, J. S. George, and B. D. Rao, "Neuromagnetic source imaging with FOCUSS: A recursive weighted minimum norm algorithm," *Electroencephalogr. Clin. Neurophysiol.*, vol. 95, no. 4, pp. 231–251, Oct. 1995.

[28] A. Tarantola, *Inverse Problem Theory and Methods for Model Parameter Estimation*. Philadelphia, PA, USA: SIAM, 2005.

[29] C. Phillips, J. Mattout, M. D. Rugg, P. Maquet, and K. J. Friston, "An empirical Bayesian solution to the source reconstruction problem in EEG," *NeuroImage*, vol. 24, no. 4, pp. 997–1011, Feb. 2005.

[30] D. Wipf and S. Nagarajan, "A unified Bayesian framework for MEG/EEG source imaging," *NeuroImage*, vol. 44, no. 3, pp. 947–966, Feb. 2009.

[31] J. Liu, Y. Kuga, A. Ishimaru, X. Pi, and A. Freeman, "Ionospheric effects on SAR imaging: A numerical study," *IEEE Trans. Geosci. Remote Sens.*, vol. 41, no. 5, pp. 939–947, May 2003.

[32] H. Brauer, M. Ziolkowski, and J. Haueisen, "Verification of the boundary element method with magnetostatic field calculations and bioelectric source reconstruction," *IEEE Trans. Magn.*, vol. 37, no. 5, pp. 3321–3324, Sep. 2001.

[33] R. Leahy, J. Mosher, M. Spencer, M. Huang, and J. Lewine, "A study of dipole localization accuracy for meg and EEG using a human skull phantom," *Electroencephalogr. Clin. Neurophysiol.*, vol. 107, no. 2, pp. 159–173, 1998.

[34] D. Kim, J. Jeong, S. Jeong, S. Kim, S. C. Jun, and E. Chung, "Validation of computational studies for electrical brain stimulation with phantom head experiments," *Brain Stimulation*, vol. 8, no. 5, pp. 914–925, Sep. 2015.

[35] N. Jekic, L. Ding, R. Dzwonczyk, and J. Raman, "Development of a physical phantom for electrocardiographic imaging validation," *J. Electrocardiol.*, vol. 43, no. 6, pp. 637–647, Nov. 2010.

[36] P. G. Stevenson, K. J. Jamison, P. R. Johnston, and M. A. Green, "Development and validation of a human thorax phantom for the assessment of cardiac electrical activity," *J. Electrocardiol.*, vol. 43, no. 6, pp. 599–605, Nov. 2010.

[37] Aichi Steel Corporation. (2025). *MI Sensor Type DJ*. [Online]. Available: https://www.aichi-steel.co.jp/ENGLISH/smart/mi/products/type-dj.html

[38] T. J. Mohun and R. H. Anderson, "3D anatomy of the developing heart: Understanding ventricular septation," *Cold Spring Harbor Perspect. Biol.*, vol. 12, no. 11, Nov. 2020, Art. no. a037465.

[39] A. van Oosterom, "ECGSIM: An interactive tool for studying the genesis of QRST waveforms," *Heart*, vol. 90, no. 2, pp. 165–168, Feb. 2004.

[40] J. Coll-Font, B. Burton, J. Tate, B. Erem, D. J. Swenson, D. Wang, D. H. Brooks, P. V. Dam, and R. MacLeod, "New additions to the toolkit for Forward/Inverse problems in electrocardiography within the SCIRun problem solving Environment," in *Proc. Comput. Cardiol.*, Sep. 2014, pp. 213–216.

[41] C. H. Wolters, L. Grasedyck, and W. Hackbusch, "Efficient computation of lead field bases and influence matrix for the FEM-based EEG and MEG inverse problem," *Inverse Problems*, vol. 20, no. 4, pp. 1099–1116, Aug. 2004.

[42] R. MacLeod, O. Weinstein, J. D. D. S. Germain, D. H. Brooks, C. R. Johnson, and S. Parker, "SCIRun/BioPSE: Integrated problem solving environment for bioelectric field problems and visualization," in *Proc. 2nd IEEE Int. Symp. Biomed. Imag., Nano Macro*, Apr. 2005, pp. 640–643.

[43] G. Stroink, "Forty years of magnetocardiology," in *Proc. 17th Int. Conf. Biomagnetism Adv. Biomagnetism–Biomag*, Mar. 2010, pp. 1–8.

[44] B. A. Steinberg, A. Roguin, S. P. Watkins, P. Hill, D. Fernando, and J. R. Resar, "Magnetocardiogram recordings in a nonshielded environment–reproducibility and ischemia detection," *Ann. Noninvasive Electrocardiol.*, vol. 10, no. 2, pp. 152–160, 2005.

K. V. ANU received the B.Tech. degree in electronics and biomedical engineering from the Model Engineering College, Thrikkakara, Kerala, India, in 2020, and the M.Tech. degree in biomedical instrumentation and signal processing from the Amrita School of Engineering, Amrita Vishwa Vidyapeetham, Amritapuri Campus, Kerala, in 2023. Currently, she is pursuing the Ph.D. degree in biomagnetism with the Department of Biomedical Engineering, Manipal Institute of Technology, Manipal Academy of Higher Education, Manipal, Karnataka, India. Her research interests include mathematical modeling, electronics circuiting, and signal and image processing.

H. RESHMA received the B.E. degree in electronics and communication engineering from The National Institute of Engineering, Mysuru, India, and the M.Tech. degree in VLSI design and embedded systems from the Department of PG Studies, Visvesvaraya Technological University, Belagavi, India. She is currently pursuing the Ph.D. degree in bio-electromagnetism. From December 2020 to November 2021, she was a Guest Lecturer in M.Sc. cybersecurity with the Department of Electronics, Mangalore University. Currently, she is a Junior Research Fellow (JRF) with the Department of Electronics and Communication Engineering, Manipal Institute of Technology, Manipal, India. Her research interest includes bio-electromagnetism.

VIKAS R. BHAT was born in Hassan, Karnataka, India, in 1993. He received the M.Tech. degree in biomedical engineering and the Ph.D. degree from the Department of Electronics and Communication Engineering, Manipal Academy of Higher Education, Manipal, India, in 2014 and June 2021, respectively. He is currently an Assistant Professor with the Department of Biomedical Engineering, Manipal Academy of Higher Education. His research interests include biomedical signal processing, bio-electromagnetism, inverse problems, and Bayesian inference.

H. ANITHA (Member, IEEE) received the B.E. degree in electronics and communication engineering from Kuvempu University, in 2001, the M.Tech. degree in computer science and engineering from Manipal University, in 2005, and the Ph.D. degree from the Department of Biomedical Engineering, Manipal University, in 2012. She is currently a Professor with the Computer Science and Engineering Department, Manipal Institute of Technology, Manipal. She has more than 12 years of experience. She received the core research grant from DST-SERB India for three years to conduct research on medical image registration for clinical applications. She has received grants from SERB-SUPRA and ICMR. Her research interests include biomedical signal, medical image processing, and medical image registration.

• • •